

A Polarization Insensitive Wide-Band Perfect Absorber

Habibe Durmaz,* Arif E. Cetin,* Yuyu Li, and Roberto Paiella

In this article, a wide-band and polarization-insensitive perfect absorber composed of 4 sandwiched layers of dielectric and metal disks is introduced. Compared to classical perfect absorbers, the system supports near-unity absorption within a wider spectral window through multiple perfect absorption mechanisms that exist due to a constituting inter-metal disk, functioning either as a dipolar antenna or a conducting ground for different perfect absorption mechanisms. Circular shape of the antenna makes the working mechanism of the system polarization insensitive. The working principle of the system is investigated through near- and far-field calculations by finite difference time domain (FDTD) simulations. A fine-tuning mechanism of the wide-range perfect absorption window is introduced through geometrical device parameters. The multilayer perfect absorber system is fabricated through a high-quality fabrication method based on electron beam lithography, lift-off method, and multi-step deposition of metal and dielectric layers. The spectral behavior of the perfect absorber system is finally experimentally investigated through Fourier transform infrared (FTIR) spectroscopy.

first MM based perfect absorber (PA), consisting of a metallic split ring and a cut wire, with 88% absorbance.^[8] Different geometries have been designed to achieve perfect absorption in different frequency ranges from visible to microwave, for example, nano-particles or apertures, ring resonators.^[9–11] Compared to these systems with perfect absorption in a narrow spectral window, systems with perfect absorption in a broad spectral range are more favorable. Consequently, wide-band MMs have been offered in different frequency ranges, using nano-features and cut-wires.^[12–15] Wide-band perfect absorption has been also achieved by designing systems with multiple narrow optical responses.^[4,16–18] The bandwidth of MM absorption spectra have been also widened by other methods, such as using resistive films,^[19] loading with lumped elements,^[20] stacking multi-layer structure,^[21] and applying magnetic medium.^[22]

1. Introduction

Metamaterials (MMs) have strong potential due to their ability to exhibit exceptional physical properties, for example, negative refractive index,^[1] invisibility cloaking,^[2] and cross polarization conversion.^[3] Adjusting electric permittivity (ϵ) and magnetic permeability (μ) of MMs, it could be possible to match the impedance of the MMs to the free space impedance, $z = \sqrt{\mu/\epsilon} = 1$, to maximize the absorption. Particularly, MMs with perfect absorption are very promising in a wide range of the fields, that is, sensors,^[4] pyroelectric detection,^[5] solar energy harvesting,^[6] and optical filters.^[7] Landy et al. have shown the

Recently, a silicon nanowire system has been proposed to achieve near-unity absorption from far-UV to near-IR wavelength ranges.^[23] Perfect absorption has been even shown with sound waves.^[24]

Here, we introduced a wide-band and polarization-insensitive PA system employing double dielectric spacers. The system is composed of 4 sandwiched disks with the order of metal, dielectric, metal, and dielectric on top of a conducting layer. Possessing two perfect absorption mechanisms thanks to the inter-metal disk in between double dielectric spacer, functioning both as a dipolar antenna and a conducting ground, the system supports two absorption peaks. Tuning the constructive interactions between the two absorption mechanisms, near-unity absorption could be observed in a wider spectral window compared to the conventional PA systems. The double-spacer PA system utilizes disk antennas, symmetric in all direction, that is, the system is polarization insensitive, eliminating the need for polarizers and providing an alignment insensitive design that can utilize the total power of the incident light. We theoretically investigated the wide-band perfect absorption mechanism of the system through finite difference time domain (FDTD) simulations. We showed the dependence of the spectral behavior of the perfect absorption on the geometrical device parameters. Finally, we fabricated the system through multi-step deposition of dielectric and metal layers, electron beam lithography (EBL), and lift-off process. We investigated the experimentally realized double-spacer PA system through Fourier transform infrared (FTIR) spectroscopy. Providing perfect absorption in a wider spectral range could be very advantageous for applications demanding strong and consistent

Dr. H. Durmaz
Department of Electrical and Electronics Engineering
Karamanoglu Mehmetbey University
Yunus Emre Yerleşkesi, Karaman 70100, Turkey
E-mail: hdurmaz@kmu.edu.tr

Dr. H. Durmaz, Y. Li, Prof. R. Paiella
Department of Electrical and Computer Engineering
and Photonics Center
Boston University
8 Saint Mary's Street, Boston, Massachusetts 02215, USA

Dr. A. E. Cetin
Izmir Biomedicine and Genome Center,
35340 Balçova, Izmir, Turkey
E-mail: arifengin.cetin@ibg.edu.tr

 The ORCID identification number(s) for the author(s) of this article can be found under <https://doi.org/10.1002/adem.201900188>.

DOI: 10.1002/adem.201900188

absorption at particular wavelengths, that is, bio-chemical detection, band-pass filters, solar cells, or imaging.

In the literature, many different double-band PA platforms have been introduced. For some of those structures, the overall absorption response arises via the superposition of the two independent absorption mechanisms (originating from 2 independent plasmonic components) that yield two spectrally isolated (spectrally apart from each other) and independently tunable absorption peaks.^[25] Moreover, other double-band PA schemes are available, where the 2 absorption peaks are due to 2 plasmonic modes excited by the cavity modes of complex nanostructures.^[26–28] The absorption peaks of these modes are spectrally isolated as the former one but could be tuned simultaneously as the 2 plasmonic modes locally interact, that is, this interaction could vary based on the tuning mechanism. Here, the main difference between these systems and double-spacer PA is the double-spacer PA system's ability to allow constructive or destructive interaction between two absorption mechanisms, providing a near-unity absorption regime between the absorption peaks.

2. Experimental Section

2.1. Working Mechanism of the Double-Spacer PA System

The unit cell of the compact structure is shown in **Figure 1a**. The PA system is composed of sandwiched 4 layers, Al, SiO₂, Al, SiO₂, on top of a thick Al layer. The disk shaped sandwiched layers have thicknesses $b_1 = 30$ nm, $a_2 = 40$ nm, $b_2 = 25$ nm, and $a_3 = 40$ nm. The thickness of the bottom Al film is $a_1 = 200$ nm. Radius of the disks and array periodicity is 400 and 1000 nm, respectively. The polarization and propagation directions of the incident wave are along the x - and z -axes, respectively. The theoretical calculations have been performed through FDTD simulations, where periodic boundary conditions are used perpendicular to the x - y plane and perfectly matched layer (PML) boundary condition is applied along the z -axis. In **Figure 1B**, the calculated absorption spectra of a classical PA (with single spacer) and the double-spacer PA are denoted with red and black curves, respectively. A near-unity absorption was obtained at two different spectral locations for double-spacer PA system, for example, $\lambda_1 = 2800$ and $\lambda_2 = 3500$ nm with 99.98% absorption and for single spacer PA system, only one near-unity absorption peak was observed at 3100 nm with 99.98% absorption.

In order to understand the physical origin of the two near-unity absorption peaks, we computed the charge distributions at these particular spectral locations. In classical PA systems, due to the dielectric spacers, near-field couplings between the metallic antennas and the bottom conducting layer induce mirror image charges on the conducting layer, resulting in anti-parallel currents that create a magnetic dipole. On the other hand, the incident light radiation polarizes the antennas along the opposite ends. The generated electric and magnetic dipoles by polarization and current loop tune permittivity and permeability to match with those of free-space, minimizing reflection while transmission is prevented by the conducting layer so that the near-unity absorbance is achieved.^[29] In the double-spacer PA system, the inter-metal disk functions as a

dipolar antenna for the bottom conducting ground while functioning as a conducting ground for the top metal antenna. Therefore, in the double-spacer PA system, we have 2 classical single-spacer PA systems, in other words 2 perfect absorption mechanisms denoted as Ab.1 and Ab.2 in **Figure 1B** – inset, interacting with each other. **Figure 1C** and **D** shows the cross-sectional charge distributions calculated at the wavelengths λ_1 and λ_2 , respectively. The mirror image charges of the top antenna on the inter-metal antenna and the mirror image charges of the inter-metal antenna on the conducting layer induce 2 anti-parallel currents on 2 planes, generating two magnetic dipoles. Having two electric dipoles with 2 magnetic dipoles generates 2 absorption peaks. As shown in the following sections, using the geometrical device parameters we could tune the interference between these dipoles, resulting in constructive or destructive effects on the perfect absorption. The electric field intensity distributions also show that the local electromagnetic fields are concentrated at the bottom and top dielectric spacers for the absorption peaks located at λ_1 and λ_2 , respectively (**Figure 1E** and **F**).

2.2. Fabrication of the Double-Spacer PA System

Figure 2A shows the fabrication scheme of double-spacer PA system, which is based on electron beam lithography (EBL) and lift-off process. The PA arrays were fabricated over a $100 \times 100 \mu\text{m}^2$ area on a Si chip. i) First, 5 nm Ti and 200 nm Al were deposited onto the Si substrate with a E-beam evaporator (Angstrom EvoVac). ii) For EBL, a positive resist, polymethyl methacrylate (950 PMMA A6, MicroChem) was spin-coated over the Al layer and EBL was performed with Zeiss SUPRA 40VP electron microscope. The EBL patterns were developed with a methyl isobutyl ketone (MIBK) – isopropanol (IPA) solution (MIBK:IPA = 1:3). iii) Later, 30 nm SiO₂, 40 nm Al, 25 nm SiO₂, and 40 nm Al, were deposited onto the developed substrate with 5 nm Ti adhesion layer prior to Al film. All materials are from Kurt J. Lesker with 99.999% purity. iv) Finally, the layers on the resist were lifted off with acetone and IPA leaving the patterned arrays of 4 sandwiched dielectric and metal layers. Oxygen plasma cleaning was performed with PVA Ted Pella America M4 plasma asher to remove any remaining residues on the surface. Scanning electron microscope (SEM) images of the fabricated samples show well-defined sandwiched double-spacer PA structures (**Figure 2B**). An atomic force microscopy (AFM) analysis (**Figure 2C**) shows that the surface roughness is 7.5 nm (root mean square). We are currently working on improving our fabrication process to produce smoother films so that the experimentally realized structures are closer to the designed ones. There are 2 main sources of roughness in the present samples. The first one is the deposition of SiO₂ with an E-beam evaporator, which could be improved with commercially available techniques, for example, low pressure chemical vapor deposition. The second one is the grain size of Al in the metal deposition step.

3. Results and Discussions

In the classical PA systems, geometrical parameters are crucial for obtaining perfect absorption and controlling their spectral

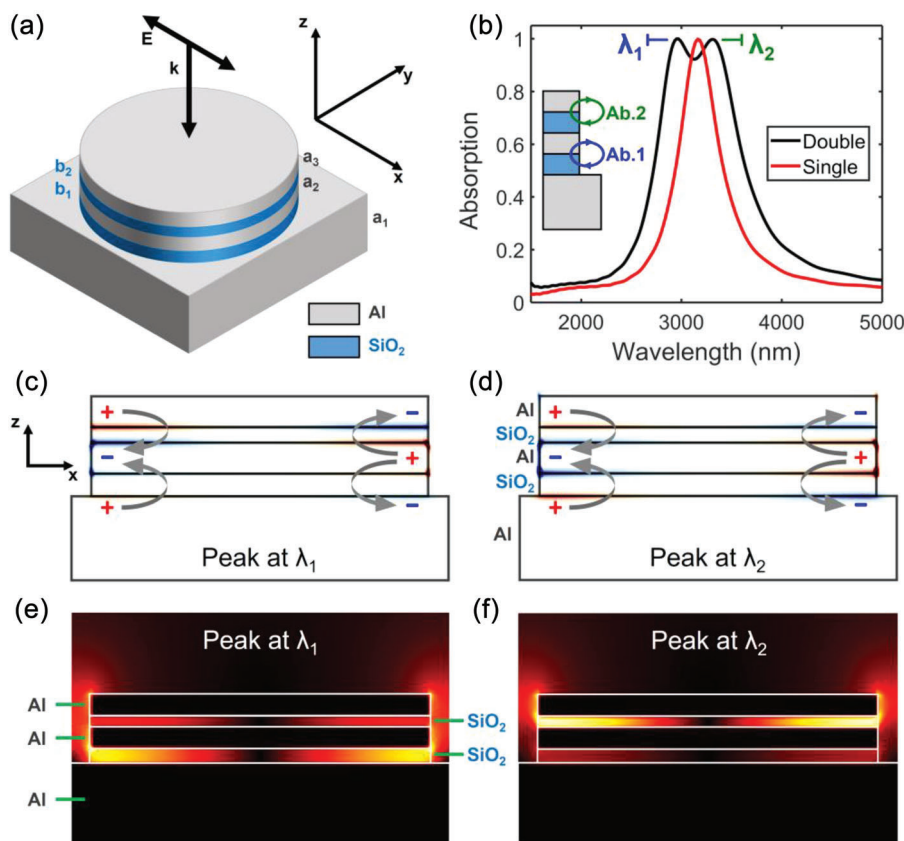


Figure 1. a) Schematic illustration of the double-spacer PA system. Propagation and polarization directions of the incident light source are indicated in the figure. b) Calculated absorption spectra of the single- (red curve) and double-spacer (black curve) PA systems. Figure inset: Schematic illustration of the 2 absorption mechanisms, playing the dominant role for the 2 absorption peaks in the double-space PA system (Ab.1 for λ_1 and Ab.2 for λ_2). Charge distributions calculated at (c) λ_1 and (d) λ_2 . The generated current loops between metal layers are indicated with gray arrows. Electric field intensity distributions calculated at (e) λ_1 and (f) λ_2 . The corresponding device parameters are $a_1 = 200$ nm, $a_2 = 40$ nm, $a_3 = 40$ nm, $b_1 = 30$ nm, $b_2 = 25$ nm, radius of the disks = 400 nm, and array periodicity = 1000 nm. For the classical PA system, Al and SiO₂ layers labeled with a_3 and b_2 , respectively were omitted from the double-spacer PA system and the rest of the geometrical parameters are common.

positions as inter- and intra-unit interactions directly depend on the dimension.^[30] In our double-spacer PA platform, in addition to these interactions, utilizing geometrical device parameters, we can also tune the interference between the 2 perfect absorption mechanisms, affecting the line-width and the shape of the absorption spectra.

3.1. Tuning PA Response with Disk Radius

Spectral tuning could be done statically, for example, via varying geometrical device dimensions^[4] or dynamically, for example, using phase changing materials.^[31,32] In order to keep our platform less complex, introducing such index-change materials, that is, phase changing materials or liquid crystal is omitted and we tuned the optical responses by changing the geometry of the PA system. In **Figure 3**, we investigate the effect of the disk radius on the absorption spectra of the double-spacer PA system. Figure 3a shows that increasing disk radius shifts both absorption peaks toward longer wavelengths. Figure 3b shows the linear correlation between disk radius and spectral position

of the absorption peaks. A similar behavior has already been shown before with nanorod and ring antennas, where the resonance wavelength of the first order dipolar plasmonic excitations has a linear correlation with the length of the rod or ring radius (L), $\lambda_{\text{res}} = 2Ln_{\text{eff}} + C$, where C is a constant and n_{eff} is the effective refractive index of the surrounding medium composed of the supporting substrate under the antennas and the medium in the vicinity,^[33,34] while the reflectance of the nanorod increases with L . For smaller radius, as the 2 dipolar antennas still function with lower reflection amplitude that occur at lower wavelength, the two absorption peaks could be still observed but lower absorption spectrally located at lower wavelengths. Here, the slope of the spectral position – disk radius relation for λ_2 (Slope = 8.8) is larger than for λ_1 (Slope = 8.3). In other words, the absorption peak at λ_2 shifts faster than the one at λ_1 , separating the two absorption peaks so that the overall absorption spectrum is getting wider by increasing disk radius. Like in the classical PA systems, in our double-spacer PA system, the dimension of the nano-antennas plays an important role to achieve the critical coupling condition between the electrical and magnetic dipoles for perfect

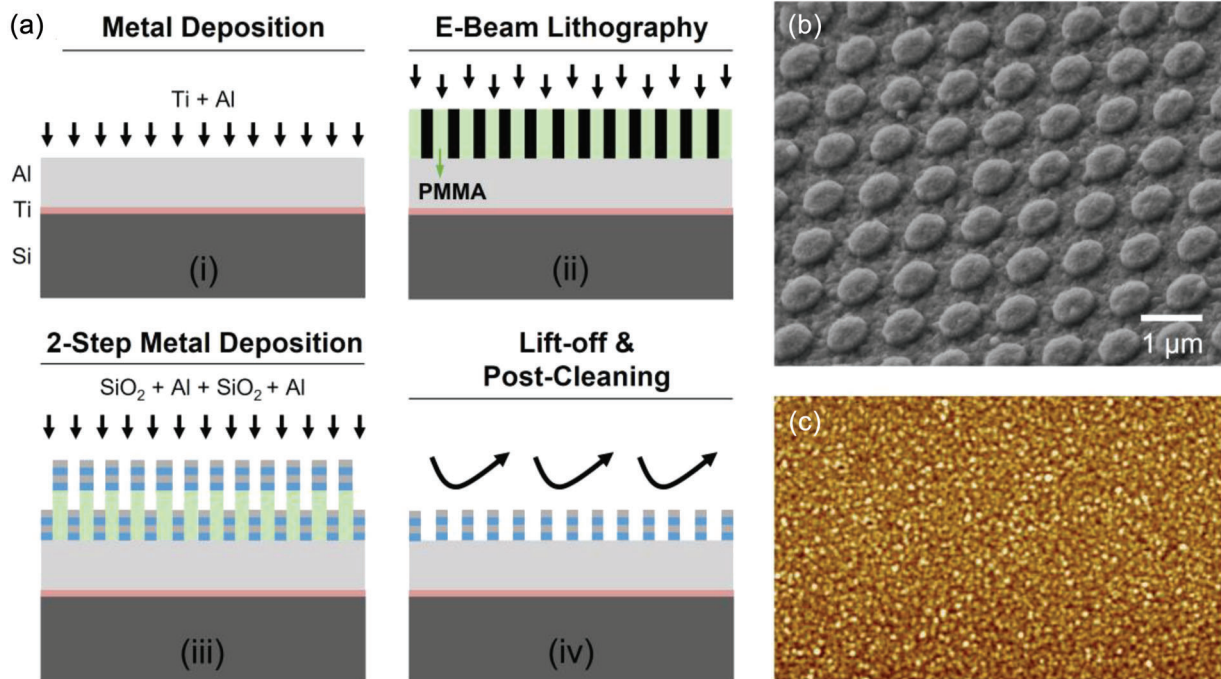


Figure 2. a) Schematic illustration of the fabrication method based on EBL, lift-off process, and consecutive steps of dielectric and metal deposition. b) SEM image of the fabricated double-spacer PA system. c) AFM image of the system showing the surface roughness.

absorptions.^[30] Therefore, in addition to the aforementioned effect, increasing the disk radius strengthens the absorption and increases its amplitude, while widening its line-width up to disk radius 400 nm. Here, 400 nm disk radius yields the optimal perfect, where the intensity of the two resonance absorption peaks is maximized. As shown in Figure 3a, after this disk radius, absorption decreases as the overlap between electric and magnetic dipole plasmon resonances decreases.

3.2. Tuning PA Response with Dielectric Spacers' Thicknesses

In Figure 4, we investigate the spectral variations of the absorption peaks with respect to the thicknesses of the 2

dielectric spacers. Figure 4a shows the variations with the thickness of the spacer between inter-metal disk and the conducting layer (b_1) while b_2 is kept constant at 25 nm. Since the local electromagnetic fields concentrate at the bottom spacer for the absorption peak at λ_1 , b_1 variations mainly affect this absorption peak, while the peak at λ_2 shows negligible changes. Here, the optimum b_1 thickness was found as 40 nm, where the spectral dip between 2 absorption peaks is maximized and the near-unity absorption was observed over a wide range. Here, for the b_1 thicknesses, for example, 15, 20, and 35 nm, due to the destructive interference between two perfect absorption mechanisms, the dominant absorption peak at λ_2 remains, while the mode at λ_1 completely disappears. Figure 4b shows the spectral variations of the absorption peaks with b_2 , while b_1 is kept constant at 30 nm. The figure

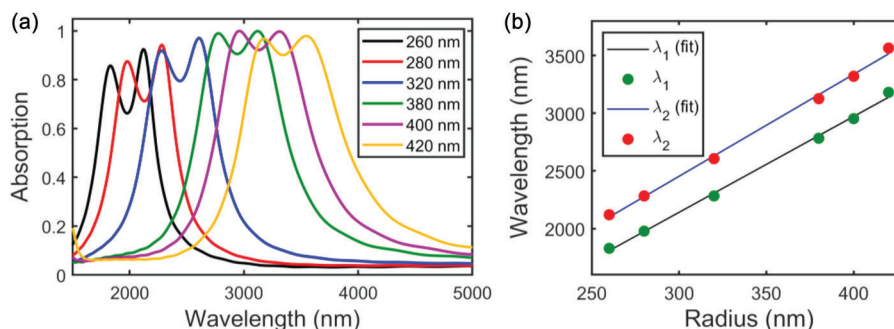


Figure 3. (a) Spectral variations in the calculated absorption spectra for different values of the disk radius. (b) Spectral locations of the 2 absorption peaks (green dots: λ_1 and red dots: λ_2) with respect to disk radius, and linear fits to the spectral location–disk radius relationship (black line: λ_1 and blue line: λ_2). The corresponding device parameters are $a_1 = 200$ nm, $a_2 = 40$ nm, $a_3 = 40$ nm, $b_1 = 30$ nm, $b_2 = 25$ nm, and array periodicity = 1000 nm.

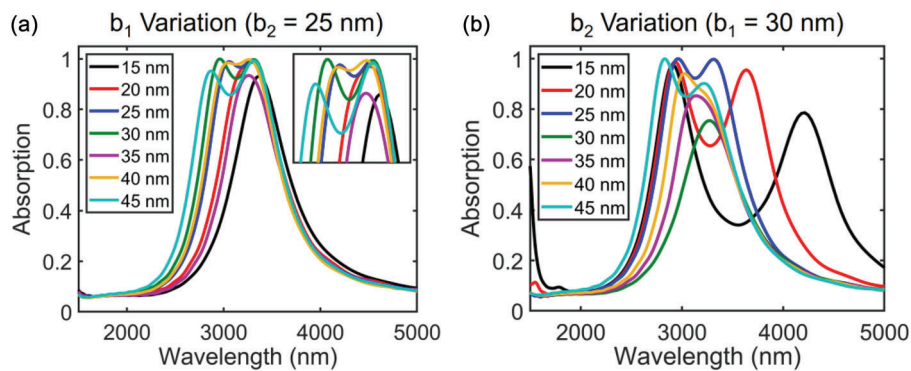


Figure 4. Spectral variations within the calculated absorption spectra of the double-spacer PA system (a) with respect to b_1 , where b_2 is kept constant at 25 nm, and (b) with respect to b_2 , where b_1 is kept constant at 30 nm. The corresponding device parameters are $a_1 = 200$ nm, $a_2 = 40$ nm, $a_3 = 40$ nm, radius of the disks = 400 nm, and array periodicity = 1000 nm.

demonstrates the fact that the absorption peak at λ_2 varies, while the one at λ_1 shows negligible variations since for the mode at λ_2 , electric field localization is concentrated at the dielectric spacer between the top and inter-metal disks. Here, for b_2 from 15 to 25 nm, the interference between the 2 perfect absorption mechanisms strengthens more such that the spectral dip between the 2 absorption peaks increases. In addition, for b_2 from 15 to 25 nm, increasing the thickness of the top dielectric spacer also brings the system to the critical coupling state for the second perfect absorption mechanism (Ab.2), increasing the absorption for the mode at λ_2 .^[30] For b_2 from 30 to 40 nm, the mode at λ_1 disappears and a single absorption peak was observed at λ_2 . Finally, at $b_2 = 45$ nm, the constructive interference between the two absorption mechanisms arises again and results in two absorption peaks.

3.3. Experimental Investigation of the Double-Spacer PA System

Finally, we performed FTIR measurements to experimentally demonstrate the absorption capability of our double-spacer PA system. The absorption spectra were measured with a Bruker Vertex FTIR spectrometer that is coupled to a Hyperion 1000 IR

microscope with a mirror velocity of 20 kHz and 256 scans. The measured optical response of the PA system was normalized to the background signal obtained from an Al reference mirror. In the experimental realization of the system (**Figure 5a**), we observed a broad near-unity absorption peak with dramatically improved line-width compared to the classical PA system. In particular, the near-unity absorption spectral window (defined as the range where the absorption drops below 97%) is found as 270 nm for the double-spacer PA system whereas it is 85 nm for the conventional PA system (not shown here). The experimentally observed behavior of Figure 5a (with a single broad peak instead of two distinct features) is actually even more favorable than the one calculated with FDTD simulations. The main difference between real and designed PA systems is the rounded shape of the disk corners instead of sharp ones as in the designed system and the surface roughness as explained before. On the other hand, in the experimentally realized system, the fine-tuning mechanism of the absorption spectra based on the interference between the 2 absorption mechanisms explained earlier could not be clearly observed due to fabrication imperfections, that is, to control the detailed shape of the absorption peaks is challenging with our current fabrication process. Therefore, we are working on our fabrication procedure to realize PA geometries confirming with the designed structures used in the FDTD simulations.

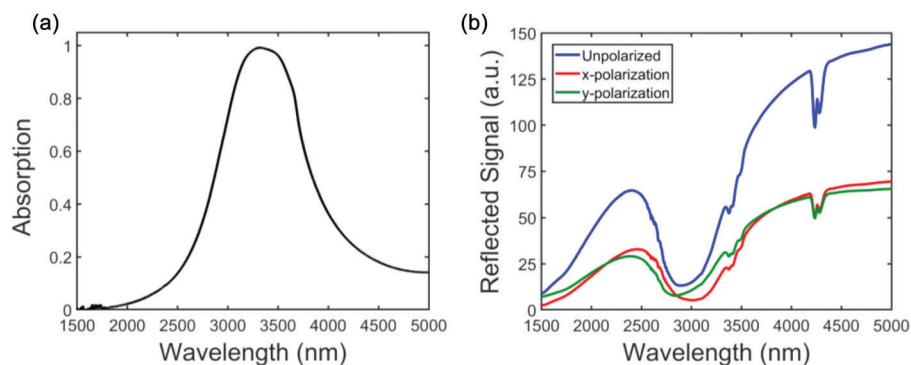


Figure 5. a) Absorption spectrum of the fabricated double-spacer PA system. b) Raw reflection data of the PA system under x- (red) and y-polarized (green), and unpolarized light sources (blue). The corresponding device parameters are $a_1 = 305$ nm, $a_2 = 39.8$ nm, $a_3 = 38.9$ nm, $b_1 = 30$ nm, $b_2 = 25$ nm, radius of the disks = 400 nm, and array periodicity = 1000 nm.

Figure 5B shows the raw reflection data, where the reflected light intensity is not normalized to that from the Al reference mirror, for unpolarized incident light (blue) and in the presence of a linear polarizer (red: x-polarized, green: y-polarized). These data illustrate the ability of the present system to provide polarization-independent near-unity absorption, which is a direct consequence of the symmetric shape of the unit cells. Here, the negligible differences between 2 polarization is the small offset in our polarizer resulting in some discrepancies from the assumed polarization angle. The fabricated structure is also not a full circle instead 5% longer in diameter along the x-axis, shifting the reflection dip toward longer wavelengths. This feature of our system eliminates the need for polarizer so that the total power of the incident light can be utilized. For sensing applications, this property is very advantageous in the presence of ultra-low concentrations of molecules needing large-intensity incident light for strong light–matter interactions.

4. Conclusion

In conclusion, we have introduced a wide-band perfect absorber system, where the plasmonic modes of the constituting antennas do not depend on the polarization direction of the incident light. The system consists of 4 sandwiched layers of dielectric and metal disks. We investigated the working mechanism of the perfect absorption through FDTD calculations. We showed that a broad, near unity absorption peak, exists due to 2 absorption mechanisms working simultaneously as the inter-metal disk functions both as a conducting layer and a dipolar antenna. We fabricated the PA system through a fabrication technique consisting of multiple steps of metal and dielectric deposition, EBL and lift-off. Finally, we showed the wide-band absorption capability of the fabricated PA system through FTIR measurements.

Acknowledgements

H.D. and A.E.C. contributed equally to this work. A.E.C. acknowledges Izmir Biomedicine and Genome Center Start-Up Research Grant. H.D. acknowledges the support of Recep Tayyip Erdogan University Scientific Research Foundation (project No: FBA-2018-892), Karamanoglu Mehmetbey University, and Boston University Photonics Center.

Conflict of Interest

The authors declare no conflict of interest.

Keywords

FDTD, perfect absorption, polarization insensitive

Received: February 19, 2019

Revised: May 18, 2019

Published online:

- [1] R. A. Shelby, D. R. Smith, S. Schultz, *Science* **2001**, 292, 77.
- [2] H. S. Chen, B. L. Wu, B. Zhang, J. A. Kong, *Phys. Rev. Lett.* **2007**, 99, 063903.
- [3] J. Y. Tang, Z. Y. Xiao, K. K. Xu, X. L. Ma, D. J. Liu, Z. H. Wang, *Opt. Quant. Electron* **2016**, 48, 111.
- [4] H. Durmaz, Y. Li, A. E. Cetin, *Sens. Actuators B* **2018**, 275, 174.
- [5] S. A. Kuznetsov, A. G. Paulish, N. C. Miguel, A. V. Arzhannikov, *Sci. Rep.* **2016**, 6, 21079.
- [6] Y. Wang, T. Y. Sun, T. Paudel, Y. Zhang, Z. F. Ren, K. Kempa, *Nano. Lett.* **2012**, 12, 440.
- [7] X. Li, L. Y. Yang, C. G. Hu, X. G. Luo, M. H. Hong, *Opt. Express* **2011**, 19, 5283.
- [8] N. I. Landy, S. Sajuyigbe, J. J. Mock, D. R. Smith, W. J. Padilla, *Phys. Rev. Lett.* **2008**, 100, 207402.
- [9] X. L. Liu, T. Starr, A. F. Starr, W. J. Padilla, *Phys. Rev. Lett.* **2010**, 104, 207403.
- [10] J. M. Hao, J. Wang, X. L. Liu, W. J. Padilla, L. Zhou, M. Qiu, *Appl. Phys. Lett.* **2010**, 96, 251104.
- [11] Q. Y. Wen, H. W. Zhang, Y. S. Xie, Q. H. Yang, Y. L. Liu, *Appl. Phys. Lett.* **2009**, 95, 241111.
- [12] C. G. Hu, L. Y. Liu, Z. Y. Zhao, X. N. Chen, X. G. Luo, *Opt. Express* **2009**, 17, 16745.
- [13] H. Wakatsuchi, S. Greedy, C. Christopoulos, J. Paul, *Opt. Express* **2010**, 18, 22187.
- [14] F. Ding, Y. Cui, X. Ge, Y. Jin, S. He, *Appl. Phys. Lett.* **2012**, 100, 103506.
- [15] F. Alves, D. Grbovic, B. Kearney, G. Karunasiri, *Opt. Lett.* **2012**, 37, 1886.
- [16] A. Tittl, P. Mai, R. Taubert, D. Dregely, N. Liu, H. Giessen, *Nano Lett.* **2011**, 11, 4366.
- [17] W. R. Zhu, Y. J. Huang, I. D. Rukhlenko, G. J. Wen, M. Premaratne, *Opt. Express* **2012**, 20, 6616.
- [18] J. Hendrickson, J. P. Guo, B. Y. Zhang, W. Buchwald, R. Soref, *Opt. Lett.* **2012**, 37, 371.
- [19] Y. Shen, Z. B. Pei, Y. Q. Pang, J. F. Wang, A. X. Zhang, S. B. Qu, *J. Appl. Phys.* **2015**, 117, 224503.
- [20] Y. Z. Cheng, Y. Wang, Y. Nie, R. Z. Gong, X. Xiong, X. Wang, *J. Appl. Phys.* **2012**, 111, 044902.
- [21] N. R. Han, Z. C. Chen, C. S. Lim, B. Ng, M. H. Hong, *Opt. Express* **2011**, 19, 6990.
- [22] H. B. Zhang, L. W. Deng, P. H. Zhou, L. Zhang, D. M. Cheng, H. Y. Chen, D. F. Liang, L. J. Deng, *J. Appl. Phys.* **2013**, 113, 013903.
- [23] J. Yang, F. Luo, T. S. Kao, X. Li, G. W. Ho, J. Teng, X. Luo, M. Hong, *Light Sci. Appl.* **2014**, 3, e185.
- [24] Y. Q. Wang, X. L. Ma, X. Li, M. B. Pu, X. G. Luo, *Opto-Electron Adv.* **2018**, 1, 180013.
- [25] E. Aslan, S. Kaya, E. Aslan, S. Korkmaz, O. G. Saracoglu, M. Turkmen, *Sens. Actuators B* **2017**, 243, 617.
- [26] T. Lu, D. Zhang, P. Qiu, J. Lian, M. Jing, B. Yu, J. Wen, S. Zhuang, *Materials* **2018**, 11, 2193.
- [27] K. Chen, R. Adato, H. Altug, *ACS Nano* **2012**, 6, 7998.
- [28] O. Ayop, M. K. A. Rahim, N. A. Murad, N. A. Samsuri, F. Zubir, H. A. Majid, *Appl. Phys. A* **2017**, 123, 63.
- [29] K. Chen, R. Adato, H. Altug, *ACS Nano* **2012**, 6, 7998.
- [30] R. Adato, A. Artar, S. Erramilli, H. Altug, *Nano Lett.* **2013**, 13, 2584.
- [31] Y. G. Chen, T. S. Kao, B. Ng, X. Li, X. G. Luo, B. Luk'yanchuk, S. A. Maier, M. H. Hong, *Opt. Express* **2013**, 21, 13691.
- [32] A. Nemat, Q. Wang, M. H. Hong, J. H. Teng, *Opto-Electron Adv.* **2018**, 1, 180009.
- [33] R. Adato, A. A. Yanik, J. J. Amsden, D. L. Kaplan, F. G. Omenetto, M. K. Hong, S. Erramilli, H. Altug, *PNAS* **2009**, 106, 19227.
- [34] A. E. Cetin, D. Etezadi, H. Altug, *Adv. Opt. Mater.* **2014**, 2, 866.